Newton

CellPress
OPEN ACCESS

Review

Characteristic frequencies in magnetic and spintronic phenomena

Atsufumi Hirohata,[1,2,3,*] Hiroki Koizumi,[1,2] Daigo Oue,[4,5,6] and Mamoru Matsuo[4,7,8]
[1]Center for Science and Innovation in Spintronics, Tohoku University, Katahira 2-1-1, Sendai 980-8577, Japan
[2]Research Institute of Electrical Communication, Tohoku University, Katahira 2-1-1, Sendai 980-8577, Japan
[3]Max-Planck-Institute for Chemical Physics of Solids, Nöthnitzer Straße 40, 01187 Dresden, Germany
[4]Kavli Institute for Theoretical Sciences, University of Chinese Academy of Sciences, Beijing 100190, P.R. China
[5]RIKEN Center for Advanced Photonics, Saitama 351-0198, Japan
[6]The Blackett Laboratory, Imperial College London, London SW7 2AZ, UK
[7]CAS Center for Excellence in Topological Quantum Computation, University of Chinese Academy of Sciences, Beijing 100190, P.R. China
[8]Advanced Science Research Center, Japan Atomic Energy Agency, Tokai 319-1195, Japan
*Correspondence: atsufumi.hirohata.d1@tohoku.ac.jp
https://doi.org/10.1016/j.newton.2025.100192

ACCESSIBLE OVERVIEW Physical phenomena are governed by their characteristic frequencies, which, in magnetism and spintronics, can cover oscillations between a few cycles per second and 10^{15} cycles per second. This range is much broader than the frequencies typically used in current devices, such as microwave ovens and mobile phones, which operate in the GHz range. This broad spectrum opens opportunities to explore a wide variety of phenomena for future device applications.

In this review, we summarize the correlations between these frequencies and the probing entities, along with their associated energies. These are primarily governed by macroscopic interactions, often dominated by magnetic anisotropy on the order of kJ/m^3. Frequencies below kHz have been studied using magnetic nanoparticles—collections of magnetic moments similar to small bar magnets—at low energies. As the energy increases, the corresponding frequency generally rises, often with fewer magnetic moments involved. Semi-classical regimes, reaching up to THz, are typically governed by exchange interactions between nuclear spins and magnetic moments, with energies on the order of μJ to mJ per m^2. These phenomena are intrinsic to specific magnetic materials and offer limited controllability through external energy input. Progressing further into the quantum regime, phenomena such as magnons and surface plasmon polaritons operate at frequencies up to PHz, involving the dynamics of a single electron spin. This is analogous to a single-electron transistor but can function at room temperature by leveraging anisotropic and exchange energies sufficient to overcome thermal fluctuation.

With ongoing miniaturization, the number of spins within a device is continually decreasing. Such reduction enables the utilization of quantum mechanical effects—such as superposition and the interference of oscillatory behaviors—leading to energy-efficient, high-frequency operation. These advancements present exciting opportunities for the development of unprecedented phenomena and devices in magnetism and spintronics.

SUMMARY

In magnetism and spintronics, a diverse array of physical phenomena is governed by distinct principles across a wide frequency spectrum. From low-frequency dynamics governed by magnetic anisotropy and nuclear spin exchange (Hz–MHz) to GHz and THz dynamics driven by exchange interactions in ferromagnets and antiferromagnets and up to PHz regimes involving surface plasmons, frequency plays a pivotal role in determining material behavior. While some of these phenomena have been experimentally realized, others remain theoretical targets. These characteristic frequencies not only reveal fundamental physics but also enable a variety of device applications. This review provides a comprehensive overview of frequency-dependent magnetic phenomena and discusses their technological implications for the first time.

INTRODUCTION

In magnetism, measurements are governed by the volume of samples under investigation.[1] The magnetic moment in a certain volume unit is one of the most sensitive measures to detect any nonmagnetic phases and disordered crystalline structures.[2,3] This is particularly critical for the macroscopic scale in a three-dimensional (3D) bulk. In a magnetic system, magnetization can be obtained as the vectorial summation of the magnetic moments of each atom. The volume of the system governs the frequency of the interactions with an external electromagnetic force, starting from the classical Brownian motion to the plasmonic interactions with an electromagnetic wave. These critical frequencies can be useful, for example, in spintronic device applications.[4] In this review, we overview the volume dependency of such critical frequencies.

MACROSCOPIC CLASSICAL INTERACTIONS

The magnetic interaction between a 3D bulk ferromagnet and an external magnetic field can be evaluated using a system consisting of ferromagnetic particles dispersed in a solution. The force F on a particle can be determined by $F = -m\nabla H$, where m is the magnetic moment of the particle and H is an applied magnetic field, which needs to exceed the resistive force by solution F_r, $F_r = 6\pi a\eta v$, where a is the radius of the particle, η is the viscosity of the solution, and v is the particle velocity. In major solutions under a magnetic field of 1 T, below 1 kHz can be used for the evaluation of the interactions between the particle and field. To move a ferromagnetic particle, the energy to be introduced by a magnetic field has to exceed the magnetic anisotropy energy E_A, which allows m to align along the field orientation as defined for the case of uniaxial anisotropy by $E_A = K_u V \sin^2\theta$ (K_u is the anisotropy constant, θ is the angle from the magnetic easy axis, and V is volume). K_u is typically on the order of kJ/m^3. In such a system, the governing dynamics is the susceptibility loss that occurs in a particle with a single magnetic domain. This induces two relaxation times associated with Néel relaxation (τ_N)[5] and Brownian relaxation (τ_B), as schematically shown in Figure 1,[6] of the particles as determined by

$$\tau_N = \frac{1}{f_0}\exp\left[\frac{KV}{k_B T}\right] \text{ and} \quad \text{(Equation 1)}$$

$$\tau_B = \frac{3V_h\eta}{k_B T}, \quad \text{(Equation 2)}$$

where $f_0 = 10^9\ s^{-1}$, K is the anisotropy constant of the particles, H_K is the anisotropy field, k_B is the Boltzmann constant, and T is the temperature of measurement. Equation 2 for the Brownian relaxation is controlled by hydrodynamic parameters, where V_h is the hydrodynamic volume. For a ferromagnetic particle with

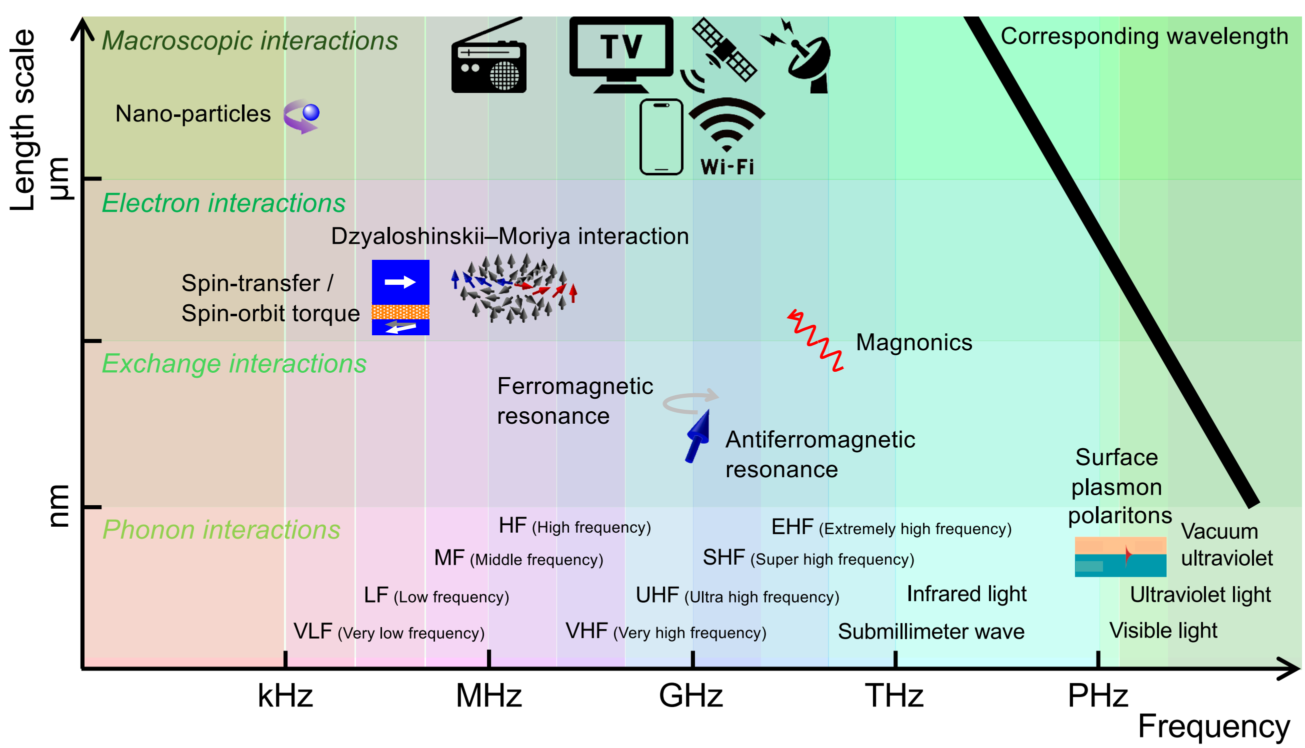

Figure 1. Frequency dependence of major magnetic and spintronic phenomena with their corresponding physical interactions
Key interactions and communication bands are listed at the representative length scales and frequencies, respectively. Some major electronic devices currently used are also shown for comparison.

a 10 nm diameter with $\eta = 1$, τ_N and τ_B can be calculated to be on the order of 10^{-9} and 10^{-4} s, respectively, corresponding to the frequency typically below the order of 10 kHz. Such classical motion of a magnetic (nano)particle has been used for magnetic hyperthermia, for example.

It is well known that the skin effect controls the penetration, skin depth δ, of an electromagnetic wave as determined by $\delta = \sqrt{2\rho/\omega\mu}$, where ρ and μ are the resistivity and magnetic permeability of a ferromagnet, respectively, and $\omega(=2\pi f)$ is the angular frequency of the electromagnetic wave at the frequency f. δ is typically on the order of μm or above at a frequency of GHz or higher. This means that to assess interactions at higher frequencies, a further reduction in nanoparticles with possible elongation and/or two-dimensional (2D) films is needed. By reducing the length scale below δ, interactions between electrons and spins within a ferromagnet cannot be ignored under an electromagnetic wave.

SEMI-CLASSICAL EXCHANGE INTERACTIONS

Ferromagnetic resonance

A magnetization $\vec{\boldsymbol{M}}$ is defined as the vector sum of the magnetic moments in a sample under investigation. The moments are aligned by the exchange interaction as determined by $E_{ex} = -2J_{ex}\sum_{i<j}\vec{\boldsymbol{S}}_i\cdot\vec{\boldsymbol{S}}_j$ (J_{ex} is the exchange integral and $\vec{\boldsymbol{S}}_i$ is the magnetic moment of an atom i). J_{ex} can be treated as an interfacial constant as a plane of magnetic moments interacting with those on the neighboring plane, typically on the order of mJ/m^2.[7] The dynamics of $\vec{\boldsymbol{M}}$ under an effective applied field $\vec{\boldsymbol{H}}_{eff}$ can be defined phenomenologically by the Landau-Lifshitz-Gilbert (LLG) equation as follows[8,9]:

$$\frac{d\vec{\boldsymbol{M}}}{dt} = -\gamma\vec{\boldsymbol{M}}\times\vec{\boldsymbol{H}}_{eff} + \frac{\alpha}{M}\vec{\boldsymbol{M}}\times\frac{d\vec{\boldsymbol{M}}}{dt}, \quad \text{(Equation 3)}$$

where γ is the absolute gyromagnetic ratio. The first term on the right-hand side of Equation 3 determines the precessional motion of $\vec{\boldsymbol{M}}$ induced by $\vec{\boldsymbol{H}}_{eff}$, which is the sum of an applied magnetic field, exchange field, anisotropic field, and so on. This continuous precession is relaxed by the second term as defined by the Gilbert damping constant α. α describes the coupling to both phonons and electrons, not just phonons (through magnon-phonon scattering and magnon-electron scattering). As a very simple approximation, α is proportional to the number of electrons available at the Fermi level, meaning the reduction for a half-metallic ferromagnet, for example. For inter-band scattering, the damping term increases with increasing temperature due to the *s-d* scattering model,[10] where conduction electrons (*s*) are scattered by localized spins (*d*) by spin relaxation, releasing the corresponding momentum into the lattice through the spin-orbit interaction. Note that at higher temperatures, α is almost proportional to the resistivity of the system ρ (resistivity-like),[11] while at low temperatures, α is proportional to the conductivity of the system σ (conductivity-like).[12] On the other hand, for intra-band scattering, Fermi surface breathing needs to be considered, resulting in the damping decreasing with increasing temperature. These two contributions have to be separated in the analysis.

The corresponding spin relaxation time τ can be calculated with approximation as[13–15]

$$\frac{1}{\tau}\sim\omega^2\tau_p\ (\text{D'yakonov} - \text{Perel model for large electron scattering probabilities})\ \text{or}$$

$$\frac{1}{\tau}\propto\frac{1}{\tau_p}\ (\text{Elliott} - \text{Yaffet model for strong spin} - \text{orbit interactions}), \quad \text{(Equation 4)}$$

where ω is the Lamor frequency and τ_p is the momentum relaxation time of an electron as determined by $\tau_p = m/ne^2\rho$ (m is the electron mass, n is the number of free electrons in a unit volume, e is the electron charge, and ρ is the resistivity). To describe the conductivity-like damping, the breathing Fermi surface model has been proposed,[16–18] which assumes non-equilibrium electronic states can be induced by the changes in magnetic moments. Typical τ_p can be calculated to be on the order of 100 fs, corresponding to the frequency on the order of GHz, which determines ferromagnetic resonance (FMR). FMR can be measured in a thin-film form using the following methods. For bulk and/or powder samples, FMR can be detected after introducing a microwave on the sample with an elevating temperature.[19]

Spin pumping (magnetization-conduction electron interactions)

In a ferromagnet/nonmagnet bilayer, a spin current can be introduced by spin pumping (SP) from the ferromagnet to the nonmagnet by precessing the ferromagnet magnetization (see Figure 2A). The spin current is damped in the nonmagnet and reduces the spin-current reflection back to the ferromagnet, increasing the damping constant of the ferromagnet. By measuring the inverse spin Hall effect (ISHE), the spin current $J_S{}^{SP}$ can be estimated as follows[20]:

$$V_{ISHE} = wR\theta_{SH}\left(\frac{2e}{\hbar}\right)J_S{}^{SP}, \quad \text{(Equation 5)}$$

where w and R are the width and resistance of the bilayered Hall bar, respectively. V_{ISHE} takes the maximum under the application of the resonant magnetic field, where the maximum precession is achieved, and the resulting maximum $J_S{}^{SP}$ is introduced to the nonmagnet. Using this condition, spin Hall angle θ_{SH} can be estimated, which is the ratio between an introduced spin-unpolarized current and a generated spin-polarized current and a measure of the spin conversion efficiency. The SP method can become sensitive to a small $J_S{}^{SP}$ by increasing R. This method can also be used for $J_S{}^{SP}$ generated either optically or thermally.

Spin torque (magnetization-conduction electron interactions)

Similar to the SP method, a ferromagnet/heavy metal bilayer has been used for a spin torque (ST-FMR) measurement. A high-frequency current I (typically at 10 GHz) is applied to the bilayer to generate an in-plane radio-frequency magnetic field H perpendicular to I in the heavy-metal layer accompanying the spin current

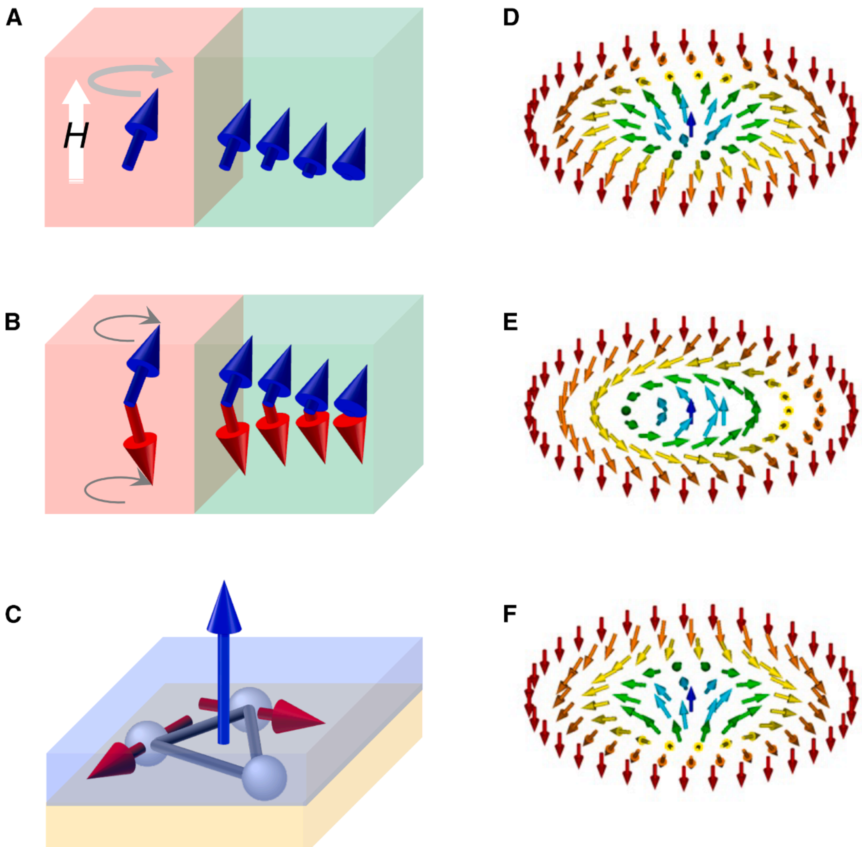

Figure 2. Schematic diagrams of spintronic phenomena that occurred at different frequencies

(A) Spin-pumping measurement in a bilayered ferromagnet/nonmagnet observed around GHz.
(B) Antiferromagnetic resonance in a bilayered antiferromagnet/nonmagnet in THz regime.
(C–F) DMI induced at a ferromagnet/heavy metal interface at MHz order (C) and the resulting magnetic skyrmions formed in three different configurations: Bloch (D), Néel (E), and anti-skyrmion (F).[4]

from the heavy-metal layer. This method was first employed to evaluate θ_{SH} in NiFe/Pt[21] and has been widely used for the measurements of θ_{SH} in a variety of materials.[22,23] Here, H exerts a torque and induces the magnetization precession in the ferromagnetic layer. At the same time, a spin current can be generated by the spin Hall effect (SHE) in the heavy metal and/or at the ferromagnet/heavy metal interface, which diffusively flows into the ferromagnetic layer and exerts a torque perpendicular to the layer. ${V_{FMR}}^{sym}$ and ${V_{FMR}}^{anti-sym}$ are given as follows[21,24]:

$${V_{FMR}}^{sym} = \frac{1}{4}\frac{dR}{d\theta}\frac{\gamma I\cos\theta}{2\pi(df/dH)_{H=H_0}}\left[\frac{\hbar {J_S}^{FMR}}{2e\mu_0 M_S t_{FM}}\frac{\Delta}{(H-H_0)^2}\right]$$

and (Equation 6)

$${V_{FMR}}^{anti\text{-}sym} = \frac{1}{4}\frac{dR}{d\theta}\frac{\gamma I\cos\theta}{2\pi(df/dH)_{H=H_0}}\left[\frac{J_C t_{AF}}{2}\left(1+\frac{e\mu_0 M_S}{\hbar}\right)^{1/2}\times\frac{(H-H_0)}{\Delta^2+(H-H_0)^2}\right],$$

(Equation 7)

where $dR/d\theta$ is the resistance change by the precession, θ is the angle between the external magnetic field and I, γ is the gyromagnetic constant, f is the frequency of I, H_0 is the FMR field, μ_0 is the magnetic permittivity in a vacuum ($4\pi \times 10^{-7}$ H/m), M_S is the saturation magnetization of the ferromagnet, t_{FM} is the thickness of the ferromagnet, Δ is the half-width of half-maximum of the FMR spectrum, t_{AF} is the AF thickness, and J_C is the charge current.

Using ${V_{FMR}}^{sym}$ and ${V_{FMR}}^{anti-sym}$, θ_{SH} can be calculated as follows[21]:

$$\theta_{SH} = \frac{{J_S}^{FMR}}{J_C} = t_{FM}t_{AF}\frac{{V_{FMR}}^{sym}}{2{V_{FMR}}^{asym}}\frac{e\mu_0 M_S}{\hbar}\sqrt{1+\left(\frac{4\pi M_{eff}}{H}\right)}.$$

(Equation 8)

By overlaying a direct current (dc) on I in the FMR method, as explained above, an effective damping constant of the ferromagnet α_{eff} can be modified as

$$\Delta\alpha_{eff} = \frac{\sin\theta}{(H+M_{eff}/2)}\frac{\hbar {J_S}^{FMR}}{2e\mu_0 M_S t_{FM}}. \quad \text{(Equation 9)}$$

By controlling I, the in-plane and perpendicular torques can be canceled out, resulting in $\Delta\alpha_{eff} = 0$. This allows oscillation of the magnetization of the ferromagnet typically at the frequency of the order of GHz at 10^{12} A/m^2.[25]

Antiferromagnetic resonance

Similar to FMR, an ST can be induced on an antiferromagnetic layer, as theoretically predicted by Núñez et al.[26] This has been experimentally demonstrated by Wei et al. by measuring the current dependence of an exchange bias field in a spin valve consisting of CoFe (10)/Cu (10)/CoFe (3)/FeMn (8) (thickness in nm), as schematically shown in Figure 2B. [27] A damping-like ST has also been calculated to induce the precessional motion of an antiferromagnetic magnetic moment, resulting in THz oscillation in a ferromagnet/antiferromagnet bilayer[28] and in a spin Hall oscillator.[29] Such THz oscillation is induced due to strong exchange interactions between two sublattices with antiparallel magnetic moments.[30,31] The first demonstration was reported in NiO, achieving up to 1 THz oscillation.[31] Since then, a great deal of research has been done to achieve higher oscillation frequencies, e.g., 13 THz,[32] in antiferromagnetic materials. SP from the antiferromagnetic layer has also been measured recently.[33] However, the spin diffusion length in the antiferromagnetic layer is measured to be on the order of a few nm.[34] For antiferromagnets, J_{ex} is typically on the order of μJ/m^2, e. g., 6 μJ/m^2 for Mn_3Sn.[35] This is almost three orders of magnitude smaller than that of a ferromagnet due to the reduction in the effective number of electrons at the Fermi level independently counted for two antiparallel magnetic moments.

Spin-transfer torque

The magnetization dynamics in a 2D film can be described using the abovementioned magnetization defined by the exchange interaction and an additional interaction between electrons as determined as a torque: spin-transfer and spin-orbit torques, for example. The spin-transfer torque (STT) is described as $\frac{\gamma}{d}\vec{\boldsymbol{m}} \times (\vec{\boldsymbol{m}} \times \Delta \vec{\boldsymbol{J}_{\mathrm{s}}})$ ($\vec{\boldsymbol{m}}$ is the unit vector of the magnetization).[36,37] By adding this term to the right side of the LLG equation (Equation 3), the magnetization dynamics can be explained.

For a particular direction of the spin current, STT is antiparallel to the Gilbert damping torque. Here, the Gauss law $\left(\frac{1}{\gamma}\frac{\partial}{\partial t}\vec{\boldsymbol{m}}\cdot V = -\int \vec{\boldsymbol{J}_{\mathrm{s}}}dS = -\Delta \vec{\boldsymbol{J}_{\mathrm{s}}}\right.$, where $V = S\cdot d$ is the volume of a ferromagnetic layer with area S and thickness $\left.d\right)$ is applied to convert the second term of the LLG equation with the STT term. This relationship indicates that the increase in the spin current $\vec{\boldsymbol{J}_{\mathrm{s}}}$ reduces the relaxation, leading to the precessional motion of magnetization yielding the switching, similar to FMR or steady-state spin-torque oscillation. Note that STT is governed by γ, which is on the order of MHz/T, resulting in the competition against the Gilbert damping at GHz.

Using such an oscillatory condition, microwave oscillations have been demonstrated in a giant magnetoresistive (GMR) nanopillar without the application of an external magnetic field.[38] In one of the pioneering works, a nanopillar consisting of an $Ni_{0.81}Fe_{0.19}$ (4)/Cu (10)/$Ni_{0.81}Fe_{0.19}$ (15) (thickness in nm) stack shows a frequency-dependent STT. A broader frequency response has been achieved for a spin-valve nanopillar of $Ni_{0.81}Fe_{0.19}$ (5)/Cu (40)/$Ni_{0.81}Fe_{0.19}$ (60) (thickness in nm) in the oscillation frequency range between 300 kHz and ∼1.1 GHz. High-frequency operation has then been extended to a tunneling magnetoresistive (TMR) nanopillar of $Co_{0.60}Fe_{0.20}B_{0.20}$/MgO/$Co_{0.60}Fe_{0.20}B_{0.20}$ with microwave generation in the vicinity of 7 GHz[39] and (3–8) GHz.[40] The frequency of these devices can be controlled by a bias current or voltage.

STT has also been used for current-induced magnetization switching to operate magnetic memories, including magnetic random access memory (MRAM) and racetrack memory,[4] fully electrically.[41] For such an operation, some layers can have a high Gilbert damping (such as the reference layer of TMR junctions, namely for MRAM), while others must exhibit a low Gilbert damping (for instance, the storage layer of MRAM or the free layer of spin-torque oscillators to minimize the required excitation current). Their operation speed is governed by the damping process at frequencies up to the GHz range, leading to <10 ns of reading/writing.[42] STT can be calculated by a critical current density for magnetization switching. A pulsed current with a duration of less than 10 ns induces adiabatic switching by a critical current density:

$$j_{\mathrm{c}} = j_{\mathrm{c0}}\left\{1 + \left(\frac{\tau_1}{\tau_{\mathrm{p}}}\right)\ln\left(\frac{\tau_{\mathrm{p}}}{\tau_0}\right)\right\} \quad \text{and (Equation 10)}$$

$$j_{\mathrm{c0}} = \alpha e M_S t\{H_{\mathrm{ext}} \pm (H_{\mathrm{a}} + 2\pi M_{\mathrm{S}})\} \big/ \hbar\left\{P \big/ \left(1 + P^2\cos\theta\right)\right\}, \quad \text{(Equation 11)}$$

where τ_p is a decreasing pulse width, τ_0 is the attempt frequency (=1 ns), τ_1 is defined as $1/\alpha\gamma(H_k + 2\pi M_{\mathrm{S}})$ (γ is an absolute gyromagnetic ratio, H_k is a uniaxial anisotropy field, and M_{S} is saturation magnetization), α is a Gilbert damping constant, e is the electron charge, t is the thickness of a ferromagnet, H_{ext} is an external magnetic field, H_{a} is a magnetic anisotropy field, $\hbar$ is the Planck constant divided by 2π, and P is the polarization of a ferromagnet.[43] Accordingly, the writing energy is sub-pJ/bit for the latest perpendicularly magnetized STT-MRAM.[43]

Similarly, a vortex core has been reported to oscillate in the frequency range between 300 kHz and 1.1 GHz in a nanopillar consisting of permalloy (60)/Cu (40)/permalloy (5) (thickness in nm).[44] Electrically switching a vortex core has been demonstrated using STT with an ac current in a 50-nm-thick permalloy disc (diameter: 1 μm).[45] In theory, these ferromagnetic discs and ferromagnet/nonmagnet/ferromagnet stacks can be operated almost up to the FMR frequency (∼ a few 10 GHz), which has significant advantages over the current Si-based devices.

Using such oscillations in a TMR junction, microwave-assisted magnetic recording (MAMR) was proposed by Zhu et al. as an approach for energy-assisted magnetic recording.[46] MAMR utilizes microwaves generated by an STT oscillator patterned in the write gap of the write head to reduce the switching field by an order of magnitude.[47] Great progress has been made lately on this technology. In 2021, Toshiba commercialized MAMR-based hard disk drives for the first time and announced further improvement in the areal density in 2025.

Spin-orbit torque

The spin-orbit interaction can be determined as

$$H_{\mathrm{SOI}} = \eta_{\mathrm{SO}}\vec{\boldsymbol{s}}\cdot\vec{\boldsymbol{L}}, \quad \text{(Equation 12)}$$

where $\vec{\boldsymbol{s}}$ and $\vec{\boldsymbol{L}}$ are the spin and orbital moments, respectively, and η_{SO} is the spin-orbit interaction constant determined as

$$\eta_{SO} = \frac{Ze^2\hbar^2}{2m^2c^3r^3}. \quad \text{(Equation 13)}$$

Here, g is the Lande g-factor, q is the electron charge, $\hbar$ is the Planck constant divided by 2π, m is the electron mass, c is the speed of light, and $\phi(r)$ is the scalar potential. Typical switching times are similar to those of STT, i.e., in a sub-GHz regime.[48]

For SOT, a critical current density for switching can be calculated using θ_{SH} as follows[49]:

$$j_c = \alpha e M_S t (H_k + 2\pi M_S) / \theta_{SH} \text{ (in} - \text{plane)}$$
and (Equation 14)

$$j_c = 2eM_S t\left\{(H_k - 4\pi M_S)/2 - H_x \Big/ \sqrt{2}\right\} \Big/ \theta_{SH} \quad \text{(perpendicular)}. \quad \text{(Equation 15)}$$

The SOT-MRAM is demonstrated to require ~10 pJ/bit for writing, which is one order of magnitude smaller than that of the latest commercial STT-MRAM.

Accordingly, SOT has been implemented in MRAM to reduce operational power consumption.[50] SOT-MRAM offers cache-compatible high speed and improved endurance at the cost of larger writing currents and footprints. In order to reduce the writing current and, consequently, the size of the selection transistor, charge-spin conversion materials with low resistivity and high SOT efficiency must be developed. To be operated in stand-alone mode, these devices require applying a static magnetic field bias.[51] SOT oscillation has been reported in a TMR junction consisting of CoFeB/MgO/CoFeB.[52] Under a magnetic field application of –160 Oe, 1.6–1.8 GHz oscillation was realized. This can potentially lead to writing speed improvement by almost 10 times as compared with STT-MRAM.

Dzyaloshinskii-Moriya interactions

Interfacial spin interaction and/or frustration can also generate geometrical phases. One example is the Dzyaloshinskii-Moriya interaction (DMI), which can be described by

$$H_{DMI} = -\vec{\boldsymbol{D}}\cdot\left(\vec{\boldsymbol{m}_i}\times\vec{\boldsymbol{m}_j}\right), \quad \text{(Equation 16)}$$

where $\vec{\boldsymbol{D}}$ is the DMI vector based on the crystalline structure.[53] It should be noted that due to the cross-product, Equation 17 contains a chirality. As shown in Figure 2C, in a ferromagnetic film with perpendicular anisotropy, the spins can rotate along either the radius or the circumference to form a vortex.[54] The difference in the rotation depends on the direction of the Dzyaloshinskii-Moriya vector, and the corresponding DMI energy density can be defined as $\left|\vec{\boldsymbol{D}}\right|\cdot\left(m_y\frac{\partial m_z}{\partial z} - m_z\frac{\partial m_y}{\partial z}\right)$, which is reported to be on the order of mJ/m^2, e.g., 2.3 mJ/m^2 for Pt/Co/MgO.[55]

A magnetic skyrmion is a topologically protected quasi-particle, as initially predicted by Skyrme,[56,57–59] consisting of a vortex configuration of magnetic spins, as shown in Figures 2D–2F. The skyrmions can be categorized into three types, Bloch, Néel, and anti-skyrmions, depending on the rotation of spins. The Bloch type continuously rotates the constituent spins across the skyrmion radius from perpendicular at the center to in-plane and back to perpendicular-to-plane on the edge, while the in-plane spin component lies along the radius. The Néel type uniformly rotates the spins with their in-plane component tangential to the radius. The anti-skyrmion combines these two types with in-plane spin rotation along the two directions.

The first observation of magnetic skyrmions was reported by Mühlbauer et al.[60] in a MnSi film. The diameter of a skyrmion (~10 nm) can be controlled by the type of material and magnetic fields, and a skyrmion can be moved by an electric current, allowing it to be used as an information career in racetrack memory.[61] In simulations, the chirality of a skyrmion can be switched by STT at a speed of <20 ns.[62] A recent report has shown that a skyrmion can be moved at a speed of up to 900 m/s, which can be converted as the spin dynamics at the frequency of GHz.[63]

QUANTUM MECHANICAL INTERACTIONS

Magnonics

By further reducing the length scale, interactions with phonons play a key role. For example, phonons can interact with magnons (spin waves) via the magnetoelastic effect. Typically, a magnet can deform 1–10 ppm under a magnetic field to align a magnetic moment $\vec{\boldsymbol{m}} = (\alpha_1, \alpha_2, \alpha_3)$ along the [100] and [111] directions to elongate λ_{100} and λ_{111}, respectively, inducing a stress vector $\vec{\boldsymbol{\sigma}} = (\gamma_1, \gamma_2, \gamma_3)$. The magnetoelastic energy can be expressed as $E_\sigma = -\frac{3}{2}\lambda_{100}|\vec{\boldsymbol{\sigma}}|\left(\alpha_1{}^2\gamma_1{}^2 + \alpha_2{}^2\gamma_2{}^2 + \alpha_3{}^2\gamma_3{}^2 - \frac{1}{3}\right) - 3\lambda_{111}|\vec{\boldsymbol{\sigma}}|(\alpha_1\alpha_2\gamma_1\gamma_2 + \alpha_2\alpha_3\gamma_2\gamma_3 + \alpha_3\alpha_1\gamma_3\gamma_1)$. The corresponding magnetoelastic constant is on the order of GJ/m^3, e.g., (1.5 ± 0.1) GJ/m^3 for a Co-ferrite, which is known to show large magnetoelastic effects.[64]

At low energy, such magnetization dynamics can be described as the oscillatory motion of $\vec{\boldsymbol{m}}$, i.e., by spin waves and their quanta, magnons. $\vec{\boldsymbol{m}}$ tied with their lattice precesses in the vicinity of its equilibrium state, the motion of which propagates along the lattice plane. Such magnon motion can be detected by Brillouin light scattering (BLS), for instance. The motion can be determined as

$$\overrightarrow{\boldsymbol{J_m}} = \hbar\sum_{\boldsymbol{k}}\overrightarrow{\boldsymbol{v_k}}\,\overrightarrow{n_{\boldsymbol{k}}}, \quad \text{(Equation 17)}$$

where $\overrightarrow{\boldsymbol{v_k}}$ is the group velocity of the spin wave ($=\partial\omega_{\boldsymbol{k}}/\partial\vec{\boldsymbol{k}}$), which is typically on the order of km/s, and $n_{\boldsymbol{k}}$ is the distribution function of the spin wave. Assuming a lattice constant of 0.2 nm for the spin-wave medium, the number of phonons in 1 km is found to be 5×10^{12}, leading to THz operation.

Under the presence of STT, a shift in precession frequency occurs similar to the Doppler effect (spin Doppler effect). The shift of spin-wave propagation in a NiFe wire under STT has been demonstrated at room temperature as the spin Doppler effect of up to 18.5 MHz.[65]

Spin caloritronics

Magnonics has experienced remarkable progress in recent years, particularly following the discovery of the spin Seebeck

CellPress
OPEN ACCESS

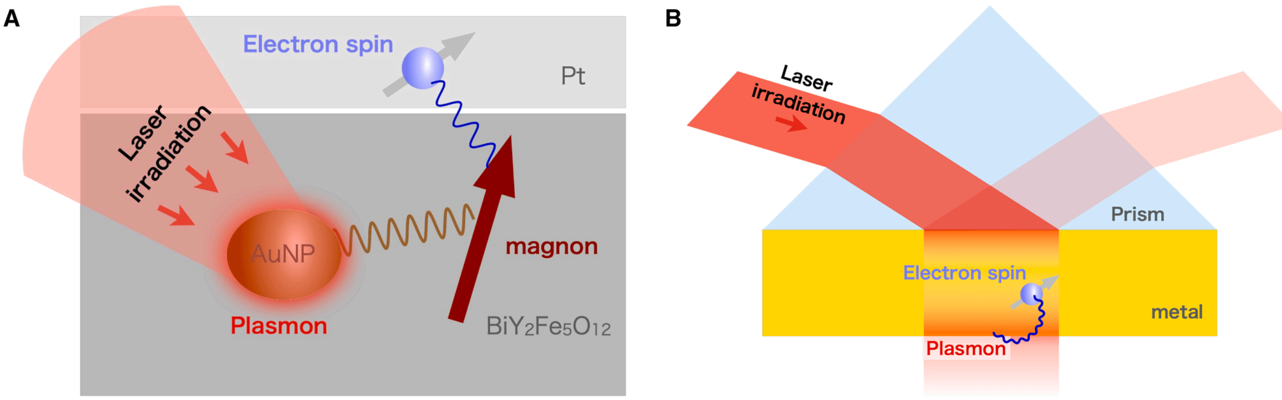

Figure 3. Schematic diagrams of optically assisted spintronic phenomena at different frequencies
(A) Plasmonic spin pumping achieved in GHz.
(B) Surface plasmon polaritons in PHz region.

effect (SSE) by Uchida et al.[66–68] This breakthrough has paved the way for extensive research in bilayer systems—typically composed of a magnetic thin film adjacent to a metal such as platinum, which exhibits strong spin-orbit interaction—where the cross-coupling between spin and heat currents leads to novel non-equilibrium transport phenomena. In these heterostructures, a temperature gradient applied across the magnetic material (for example, in a Pt/yttrium iron garnet [YIG] junction) thermally excites its magnetization, thereby generating a conduction spin current in the adjacent Pt layer through interfacial magnetic interactions. These advances have led to the emergence of "spin caloritronics," a field that focuses on the interplay between heat and spin degrees of freedom.[69]

At the heart of spin caloritronics is the SSE, a universal heat-to-spin conversion process observed in a wide range of magnetic materials, including ferromagnetic metals, insulators,[70,71] and semiconductors.[72,73] In a typical Pt/YIG junction, the temperature gradient excites the magnon population in the magnetic layer, and through interfacial interactions, this excitation is converted into a conduction spin current in the Pt film. This process is further complemented by its reciprocal counterpart, the spin Peltier effect (SPE), in which the injection of a spin current produces a measurable heat flow.[74–77] The resulting spin current, whose characteristic frequency is determined by the intrinsic magnetic and lattice dynamics, encapsulates the fundamental spin properties of the magnetic layer and has been successfully used as a quantum probe, for instance, in exploring magnetic phase transitions in thin films.[78]

The underlying mechanism of the SSE involves establishing a temperature gradient across a magnetic insulator/metal interface. This gradient leads to a difference in the effective temperatures of magnons in the magnetic insulator and electrons in the metal, creating a non-equilibrium spin accumulation at the interface. This spin accumulation, in turn, drives a spin current into the metal via interfacial exchange interactions. Building upon this fundamental understanding, techniques such as plasmonic SP and acoustic SP (which will be shown below) have been developed. These methods leverage the principle of creating non-equilibrium spin distributions across interfaces to generate spin currents. The frequency of a magnon polaron detected by SSE has been reported to be 0.16 and 0.53 THz for a transverse and a longitudinal acoustic phonon branch, respectively.[79] Theoretically, the frequency can be extended into a THz regime.[80] For the SPE, the transient response has been reported to be measured within the frequency range between 10 Hz and 1 MHz.[81]

Plasmonic SP

Another approach that utilizes non-equilibrium magnon dynamics is a method called plasmonic SP, which generates pure spin currents using optical excitation.[82–84] In this scheme, as schematically shown in Figure 3A, a bilayer device is constructed by combining a thin Pt film with a ferrimagnetic insulator (such as $BiY_2Fe_5O_{12}$). Within this heterostructure, Au nanoparticles are embedded to function as nanoscale antennas supporting localized surface plasmon resonances (LSPRs). When the device is illuminated with monochromatic light tuned to the plasmon resonance frequency, strong evanescent electromagnetic fields are produced around the Au nanoparticles. These intense fields excite non-equilibrium magnons in the adjacent magnetic layer. Through interfacial magnetic interactions, the energy and angular momentum of these magnons are transferred into the Pt layer, thereby "pumping" a pure conduction spin current. This spin current is then detected via the ISHE, which converts the spin current into a measurable transverse voltage. In Uchida et al.,[82] the spin current was reported to be generated by the introduction of light with the wavelength of 690 nm; the corresponding frequency can be estimated to be 430 PHz. Because the mechanism is driven by the optical excitation of surface plasmons, plasmonic SP represents a unique and ultrafast pathway to convert light into spin currents, offering promising applications in next-generation spintronic devices and optically controlled energy-harvesting systems. In a broader context, localized surface plasmons have been reported to induce ultrafast demagnetization,[85] dynamically control the transmission of spin waves,[86] and excite magnetic topological structures, such as skyrmions and skyrmioniums.[87]

Surface plasmon polaritons

Furthermore, as an alternative scenario for generating spin currents using propagating surface plasmons, the following new approach has been proposed. It is well known that below the plasma frequency $\omega_p = \sqrt{ne^2/\varepsilon_0 m}$ (n is the electron density, e is the electron charge, ε_0 is the permittivity in a vacuum, and m is the electron mass), only free (conduction) electrons oscillate, as the electron mass m is much smaller than that of the ionic core. In a magnetic material, m and ε_0 need to be replaced with the material-specific values of an effective electron mass m^* and permittivity ε. To be precise, the damping needs to be considered as well. The collective oscillation of conduction electrons is a fundamental excitation in the bulk of a metal, which is quantized with energy $\hbar\omega_p$. The plasma frequency ω_p is typically on the order of 1 PHz.

At a metal-insulator interface, a plasmon in the metal and a photon in the insulator are hybridized and localized, forming a polariton. Due to hybridization, the characteristic frequency is modified, $\omega_p \rightarrow \omega_{sp} = \omega_p/\sqrt{1+\epsilon_{ins}}$, where ϵ_{ins} is the permittivity of the insulator. This polariton is known as a surface plasmon polariton (SPP).[88] SPPs can be excited optically with the Otto and Kretschman-Raether arrangements (or their mixture), consisting of a prism placed on a metal/insulator bilayer without and with a gap.[89] SPPs can generate a transversely spinning electric field at the frequency of a few PHz, according to the macroscopic electromagnetic theory with the Drude model.[90–93] For an SPP propagating in the x direction, which is localized at the metal-insulator interface ($z = 0$), the electric field inside the metal can be written as

$$\boldsymbol{E} = E_0\left(i\frac{\kappa}{\sqrt{k^2+\kappa^2}}\boldsymbol{u}_x + \frac{k}{\sqrt{k^2+\kappa^2}}\boldsymbol{u}_z\right)e^{ikx+\kappa z} \quad (z<0), \qquad \text{(Equation 18)}$$

where E_0 is the field amplitude, k and κ are the propagation and decay constants, respectively, and the vector in the parentheses represents the polarization state of the field. In the non-relativistic limit ($c \rightarrow \infty$), the decay constant is approximated as $\kappa \approx k$. With this approximation, the polarization vector can be reduced to $(i\boldsymbol{u}_x + \boldsymbol{u}_z)/\sqrt{2}$, which evidently represents a circularly polarized state (i.e., a spinning field).

Conduction electrons involved in the SPP field follow the spinning electric field; thereby, their orbiting motion generates inhomogeneous magnetic moments in the metal. According to the macroscopic electromagnetic theory, the corresponding magnetization is evaluated as follows[93–95]:

$$\vec{M} = \frac{e}{8m}\epsilon_0\frac{d\epsilon}{d\omega}\mathrm{Im}\left\{\vec{\mathbf{E}}\times\vec{\mathbf{E}}^*\right\}. \qquad \text{(Equation 19)}$$

Since the electric field brought about by the SPP decays exponentially, the induced magnetization also decays exponentially ($\vec{M} \propto \exp(2\kappa z)\vec{\mathbf{u}}_\mathbf{y}$).

By solving the diffusion equation with a source term representing the induced inhomogeneous magnetization, Oue and Matsuo have recently predicted the generation of a spin-polarized electric current.[96–98] They estimated that a spin current of 10^5 A/m^2 can be generated in Au by SPPs at 1.25 PHz. For a 20-nm-thick Au film with a laser spot size of 1 mmϕ, the resistance can be estimated as 6.1×10^{-12} Ω (resistivity of Au: 2.44×10^{-8} Ω × m), leading to the static electric power of 6.1×10^{-2} W. By using a 0.4 mW semiconductor laser, the spin conversion efficiency can be estimated to be 1.5, suggesting potentially high efficiency. Bekshaev conducted a follow-up study on spin-current generation by propagating surface plasmons on a single surface.[99] Ukhtary et al. demonstrated that surface plasmons at graphene edges can generate spin currents through a similar mechanism.[100,101] Recently, Au nanoparticles/Al_2O_3 interfaces have also been used to demonstrate spin-current generation.[102]

SP and mechanical motions

In recent years, the field of spintronics has witnessed growing interest in novel methods of spin control and spin-current generation utilizing mechanical vibrations and rotational motion.

Mechanically engineered spin temperatures

Acoustic SP[71,103,104] has been demonstrated as a method for spin injection through the modulation of effective magnetization temperature by acoustic waves. This phenomenon was experimentally verified in YIG/Pt bilayer systems, where acoustic waves in the MHz range were excited, and the generated spin current was electrically detected through the ISHE in the Pt layer. The fundamental mechanism in such magnetic/metallic bilayer systems, including the SSE[66] and SP,[82] involves spin tunneling across interfaces driven by the difference in non-equilibrium distribution functions between magnetization in magnetic materials and conduction electron spins in metals. Similar to how temperature gradients drive effective temperature differences between magnetization and conduction electron spins in the SSE, acoustic waves serve as the driving force for generating these effective temperature differences.

Elastically driven SP

Furthermore, Weiler et al. demonstrated elastically driven SP,[105–107] which represents a system analogous to conventional SP. In conventional SP within magnetic/metallic bilayers, magnetization in the magnetic layer is coherently excited through FMR to inject spins into the metal, traditionally achieved through the application of an alternating-current magnetic field. In contrast, Weiler et al. achieved SP by inducing FMR through Rayleigh-type surface acoustic waves in the magnetic material. These surface acoustic waves operate in the GHz range, matching the resonant frequency of ferromagnetic materials. The interaction between magnetization and elastic waves in this context occurs through magnetoelastic coupling. Recent studies have reported non-trivial, nonreciprocal propagation phenomena utilizing the antisymmetric components of lattice strain in magnetoelastic coupling, indicating increased research activity in spin dynamics mediated by magnetoelastic coupling.[108]

Gyromagnetic effects

The phenomena discussed thus far have involved interactions between ferromagnetic materials and mechanical vibrations. Recently, gyromagnetic effects[109–112] have emerged as methods for spin control and spin-current generation that exploit the interaction between spin and mechanical motion without requiring ferromagnetic materials.

The gyromagnetic effect, discovered in 1915 by Barnett[109] and Einstein and de Haas,[110] represents a phenomenon of interconversion between magnetization and mechanical angular momentum. Prior to the establishment of quantum theory, magnetism was believed to originate from Amperian currents due to electron orbital motion. However, experimental results from the Barnett effect (magnetization induced by rotating magnetic materials) and the Einstein-de Haas effect (mechanical rotation induced by changing magnetization) yielded a g-factor of 2. This suggested the existence of an intrinsic magnetic angular momentum in electrons that could not be explained by classical electromagnetism, later identified as spin angular momentum.[113] (Although Einstein and de Haas conducted their experimental demonstration to verify that the origin of magnetism lay in Amperian currents, Einstein initially disputed the finding that $g = 2$, maintaining that it should be $g = 1$. However, he later retracted this position and accepted that $g = 2$. This historical development provides fascinating insights into the early understanding of electron spin and magnetism, as detailed in Topper[113].)

While the original gyromagnetic effects were observed in ferromagnetic materials, these effects fundamentally arise from spin-rotation coupling[114–116] between spin and angular velocity rather than requiring ferromagnetic materials specifically. This coupling has been experimentally verified not only for electron spins[117–136] but also for nuclear spins,[137–141] quarks, gluons, and hadron spins.[142–146]

Einstein-de Haas effect

Studies of the Einstein-de Haas effect have progressed significantly through the application of micro/nanoelectromechanical systems. An experiment utilized cantilever-based measurements operating at frequencies of approximately 10 kHz to determine the g-factor of NiFe thin films.[117] Subsequently, ultra-sensitive mechanical measurements enabled the detection of itinerant electron spin flips.[118] Further advances in the field have led to the observation of ultrafast demagnetization processes on the 100 fs timescale.[119] Additional investigations demonstrated the Einstein-de Haas effect through mechanical vibrations of a cantilever, where magnon current was excited in a ferromagnetic insulator microcantilever through the SSE and subsequent magnon relaxation was detected.[135] Moreover, the Einstein-de Haas effect has been observed at radio frequencies in and near magnetic equilibrium.[120]

Barnett effect

Regarding the Barnett effect, direct measurements of effective magnetic fields generated by spin-rotation coupling in rotating nuclear spin systems were initially achieved using spinning nuclear magnetic resonance (NMR) techniques.[137–140] Similar phenomena of effective magnetic field generation due to rotation have subsequently been observed in analogous systems, including nitrogen vacancy (NV) centers.[136,141] The mechanical rotation generated in spinning NMR operates in the kHz range, whereas NMR resonant frequencies are in the MHz range. This difference enables precise measurements of the effective magnetic field, which induces resonance frequency shifts of several percent relative to the NMR frequency.

In electronic systems, the Barnett effect has been observed in paramagnetic[121,122] and ferrimagnetic[123,124] materials using mechanical rotation ranging from several kHz to tens of kHz. Later, spin-current generation through rigid rotation at kilohertz frequencies has been experimentally verified using magneto-optical detection, extending beyond mere spin polarization effects.[134]

Additionally, spin-current generation phenomena have been observed utilizing local mechanical rotation characterized by vorticity in liquid metals[125–128,147] and metal thin films with excited surface acoustic waves.[129–132] The scale of local rotation in liquid metal systems is approximately kHz, whereas the vorticity of surface acoustic waves reaches the GHz range.

An analogous phenomenon has been observed in quark-gluon plasma, where extraordinary vorticity measurements have revealed angular velocities reaching 10^{21} Hz,[142–146] representing the highest rotational motion achieved by humanity.

CONCLUDING REMARKS AND FUTURE PERSPECTIVES

As listed in Figure 4, three categories of phenomena are distributed across a broad range of frequencies between Hz and PHz. First of all, classical phenomena are governed by macroscopic interactions, which can be dominated by magnetic anisotropy. Typically, the interactions are on the order of kJ/m^3, generating a range of signal frequencies between a few Hz and a few 100 Hz, as observed in the motion of magnetic particles. By increasing the introduction energy and using semi-classical probes, a higher frequency can be generated. An exchange interaction between nuclear spins generates MHz signals, and that between magnetic moments on the order of mJ/m^2 and μJ/m^2 produces GHz and THz dynamics in parallel (ferromagnetic) and antiparallel (antiferromagnetic) configurations, respectively. These frequencies are unique to a magnetic material used with minor controllability with the energy introduced. Similarly, exchange interactions between a magnetic/spin moment and a conduction-electron spin generate ~GHz signals, which are mainly interfacial interactions on the order of mJ/m^2. Finally, a further increase in energy leads to a quantum mechanical regime, which requires the consideration of their wave nature, such as magnonics, SPPs, and elementary particles, at PHz frequency.

In order to design a new magnetic and spintronic device, one may use the energy range met with the requirements as shown in Figure 4. This naturally offers the corresponding frequency range for their operation. Among them, conduction spins can cover a broad range between MHz and THz, which can become one of the key phenomena that govern the device design. By controlling the number of such electrons and their operating temperature, one may be able to further extend the frequency ranges, resulting in more applicability of magnetism and spintronic for future device applications as well as possible discovery of new phenomena.

ACKNOWLEDGMENTS

This work was partially supported by the Japan Science and Technology Agency (JST) Core Research for Evolutional Science and Technology (CREST) project (no. JPMJCR17J5), the Japan Society for the Promotion of Science (JSPS) Grants-in-Aid for Scientific Research – Home-Returning Researcher Development Research program (no. 23K34567), the European

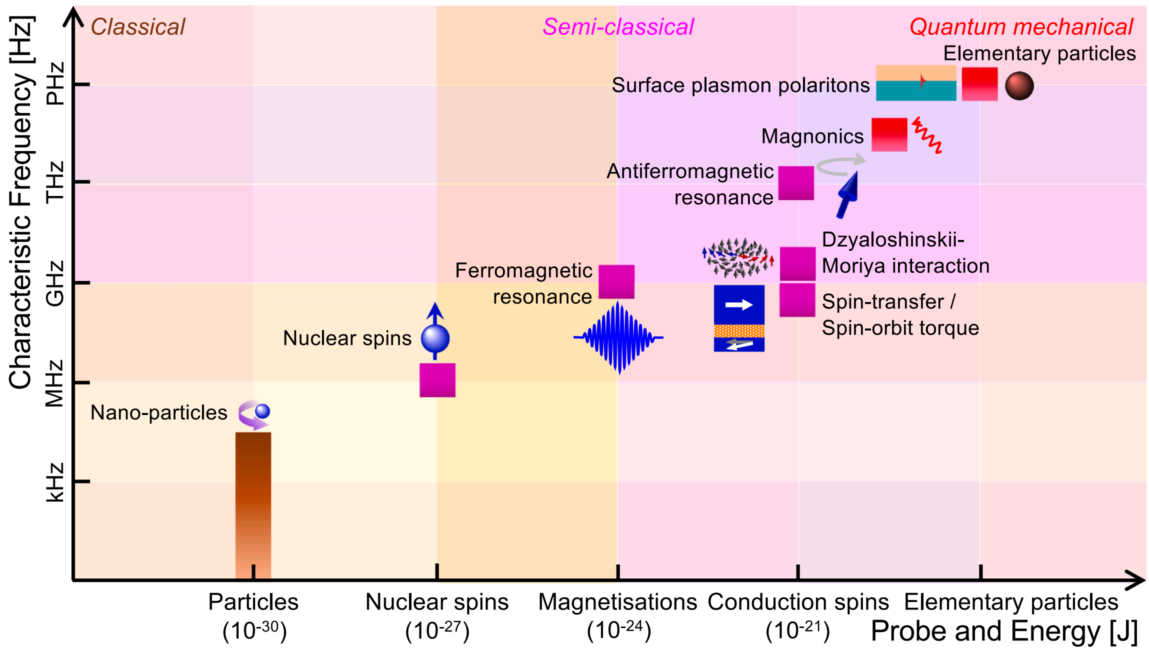

Figure 4. Energy dependence of signal frequency
Representative probes and their energies are listed for spintronic phenomena and major physical behavior as a function of their characteristic frequencies.

Commission (EC) European Research Council (ERC) Advanced Grant "Strain-Free All Heusler Alloy Junctions – SAHAJ" (no. 101097475), the National Natural Science Foundation of China (NSFC) (no. 12374126), and JSPS KAKENHI grants (nos. 23H01839 and 24H00322) from the Ministry of Education, Culture, Sports, Science and Technology (MEXT), Japan. D.O. acknowledges support from the RIKEN Institute of Physical and Chemical Research special postdoctoral researcher program.

AUTHOR CONTRIBUTIONS

A.H. initiated this review and wrote the introduction, macroscopic classical interactions, semi-classical exchange interactions, and quantum mechanical interactions: magnonics sections with H.K. D.O. was responsible for quantum mechanical interactions: surface plasmon polaritons, and M.M. was in charge of the remainder of the sections. All authors were equally responsible for the summary of this review.

DECLARATION OF INTERESTS

The authors declare no competing interests.

REFERENCES

1. Coey, J.M.D. (2010). Magnetism and Magnetic Materials (Cambridge, United Kingdom: Cambridge University Press). https://doi.org/10.1017/CBO9780511845000.
2. C. Felser and A. Hirohata, eds. (2016). Heusler Alloys (Berlin, Germany: Springer). https://doi.org/10.1007/978-3-319-21449-8.
3. Elphick, K., Frost, W., Samiepour, M., Kubota, T., Takanashi, K., Sukegawa, H., Mitani, S., and Hirohata, A. (2021). Heusler alloys for spintronic devices: review on recent development and future perspectives. Sci. Technol. Adv. Mater. *22*, 235–271. https://doi.org/10.1080/14686996.2020.1812364.
4. Hirohata, A., Yamada, K., Nakatani, Y., Prejbeanu, I.L., Diény, B., Pirro, P., and Hillebrands, B. (2020). Review on spintronics: Principles and device applications. J. Magn. Magn Mater. *509*, 166711. https://doi.org/10.1016/j.jmmm.2020.166711.
5. Néel, L. (1949). Theorie du trainage magnetique des ferromagnetiques en grains fins avec applications aux terres cuites. Ann. Geophys. *5*, 99.
6. Brown, W.F. (1963). Thermal fluctuations of a single-domain particle. Phys. Rev. *130*, 1677–1686. https://doi.org/10.1103/PhysRev.130.1677.
7. Nguyen, T.V.A., Shiratsuchi, Y., Yonemura, S., Shibata, T., and Nakatani, R. (2018). Energy condition of isothermal magnetoelectric switching of perpendicular exchange bias in Pt/Co/Au/$Cr2O_3$/Pt stacked film. J. Appl. Phys. *124*, 233902. https://doi.org/10.1063/1.5047563.
8. Landau, L., and Lifshitz, E. (1935). On the theory of dispersion of magnetic permeability in ferromagnetic bodies. Physik A (Soviet Union) *8*, 153.
9. Gilbert, T.L. (2004). A phenomenological theory of damping in ferromagnetic materials. IEEE Trans. Magn. *40*, 3443–3449. https://doi.org/10.1109/TMAG.2004.836740.
10. Mott, N.F., and Massey, H.S.W. (1965). The Theory of Atomic Collisions, Third Edition (Oxford: Oxford University Press).
11. Ma, X., Ma, L., He, P., Zhao, H.B., Zhou, S.M., and Lüpke, G. (2015). Role of antisite disorder on intrinsic Gilbert damping in $L1_0$ FePt films. Phys. Rev. B *91*, 014438. https://doi.org/10.1103/PhysRevB.91.014438.
12. Bhagat, S.M., and Lubitz, P. (1974). Temperature variation of ferromagnetic relaxation in the 3*d* transition metals. Phys. Rev. B *10*, 179–185. https://doi.org/10.1103/PhysRevB.10.179.
13. D'yakonov, M., and Perel, V. (1972). Spin relaxation of conduction electrons in noncentrosymmetric semiconductors. Sov. Phys. Solid State *13*, 3023.
14. Elliott, R.J. (1954). Theory of the effect of spin-orbit coupling on magnetic resonance in Some semiconductors. Phys. Rev. *96*, 266–279. https://doi.org/10.1103/PhysRev.96.266.
15. Yafet, Y. (1963). g factors and spin-lattice relaxation of conduction electrons. Solid State Phys. *14*, 1.

16. Kamberskỳ, V. (1970). Ferromagnetic resonance in iron whiskers. Can. J. Phys. *48*, 1103. https://doi.org/10.1139/p70-142.
17. Koreman, V., and Prange, R.E. (1972). Anomalous damping of spin waves in magnetic metals. Phys. Rev. B *6*, 2769. https://doi.org/10.1103/PhysRevB.6.2769.
18. Kuneš, J., and Kamberský, V. (2002). First-principles investigation of the damping of fast magnetization precession in ferromagnetic 3*d* metals. Phys. Rev. B *65*, 212411. https://doi.org/10.1103/PhysRevB.65.212411.
19. Whitney, A., Liu, C., Santos, T.S., Chopdekar, R.V., Carey, M., Street, G., Kalappattil, V., Leistikow, K., and Wu, M. (2023). Damping in free layers of spin-transfer-torque magnetic memory at elevated temperatures. Phys. Rev. Appl. *20*, 034006. https://doi.org/10.1103/PhysRevApplied.20.034006.
20. Ruiz-Calaforra, A., Brächer, T., Lauer, V., Pirro, P., Heinz, B., Geilen, M., Chumak, A.V., Conca, A., Leven, B., and Hillebrands, B. (2015). The role of the non-magnetic material in spin pumping and magnetization dynamics in NiFe and CoFeB multilayer systems. J. Appl. Phys. *117*, 163901. https://doi.org/10.1063/1.4918909.
21. Liu, L., Moriyama, T., Ralph, D.C., and Buhrman, R.A. (2011). Spin-torque ferromagnetic resonance induced by the spin Hall effect. Phys. Rev. Lett. *106*, 036601. https://doi.org/10.1103/PhysRevLett.106.036601.
22. Seki, T., Iihama, S., Taniguchi, T., and Takanashi, K. (2019). Large spin anomalous Hall effect in $L1_0$ – FePt: Symmetry and magnetization switching. Phys. Rev. B *100*, 144427. https://doi.org/10.1103/PhysRevB.100.144427.
23. Seki, T., Lau, Y.-C., Iihama, S., and Takanashi, K. (2021). Spin-orbit torque in a Ni-Fe single layer. Phys. Rev. B *104*, 094430. https://doi.org/10.1103/PhysRevB.104.094430.
24. Layadi, A., and Artman, J.O. (1997). Study of antiferromagnetic coupling by ferromagnetic resonance (FMR). J. Magn. Magn Mater. *176*, 175–182. https://doi.org/10.1016/S0304-8853(97)00142-X.
25. Ben-Shalom, R., Bernstein, N., Parkin, S.S.P., Yang, S.-H., and Capua, A. (2021). Determination of the spin Hall angle by the inverse spin Hall effect, device level ferromagnetic resonance, and spin torque ferromagnetic resonance: A comparison of methods. Appl. Phys. Lett. *119*, 042401. https://doi.org/10.1063/5.0057192.
26. Núñez, A.S., Duine, R.A., Haney, P.M., and MacDonald, A.H. (2006). Theory of spin torques and giant magnetoresistance in antiferromagnetic metals. Phys. Rev. B *73*, 214426. https://doi.org/10.1103/PhysRevB.73.214426.
27. Wei, Z., Sharma, A., Nunez, A.S., Haney, P.M., Duine, R.A., Bass, J., MacDonald, A.H., and Tsoi, M. (2007). Changing exchange bias in spin valves with an electric current. Phys. Rev. Lett. *98*, 116603. https://doi.org/10.1103/PhysRevLett.98.116603.
28. Gomonay, H.V., and Loktev, V.M. (2010). Spin transfer and current-induced switching in antiferromagnets. Phys. Rev. B *81*, 144427. https://doi.org/10.1103/PhysRevB.81.144427.
29. Cheng, R., Xiao, D., and Brataas, A. (2016). Terahertz antiferromagnetic spin Hall nano-oscillator. Phys. Rev. Lett. *116*, 207603. https://doi.org/10.1103/PhysRevLett.116.207603.
30. Satoh, T., Cho, S.-J., Iida, R., Shimura, T., Kuroda, K., Ueda, H., Ueda, Y., Ivanov, B.A., Nori, F., and Fiebig, M. (2010). Spin oscillations in antiferromagnetic NiO triggered by circularly polarized light. Phys. Rev. Lett. *105*, 077402. https://doi.org/10.1103/PhysRevLett.105.077402.
31. Kampfrath, T., Sell, A., Klatt, G., Pashkin, A., Mährlein, S., Dekorsy, T., Wolf, M., Fiebig, M., Leitenstorfer, A., and Huber, R. (2011). Coherent terahertz control of antiferromagnetic spin waves. Nat. Photonics *5*, 31–34. https://doi.org/10.1038/nphoton.2010.259.
32. Tzschaschel, C., Satoh, T., and Fiebig, M. (2019). Tracking the ultrafast motion of an antiferromagnetic order parameter. Nat. Commun. *10*, 3995. https://doi.org/10.1038/s41467-019-11961-9.
33. Takei, S., Moriyama, T., Ono, T., and Tserkovnyak, Y. (2015). Antiferromagnet-mediated spin transfer between a metal and a ferromagnet. Phys. Rev. B *92*, 020409. https://doi.org/10.1103/PhysRevB.92.020409.
34. Baltz, V., Manchon, A., Tsoi, M., Moriyama, T., Ono, T., and Tserkovnyak, Y. (2018). Antiferromagnetic spintronics. Rev. Mod. Phys. *90*, 015005. https://doi.org/10.1103/RevModPhys.90.015005.
35. Asakura, M., Higo, T., Matsuo, T., Uesugi, R., Nishio-Hamane, D., and Nakatsuji, S. (2024). Observation of omnidirectional exchange bias at all-antiferromagnetic polycrystalline heterointerface. Adv. Mater. *36*, 2400301. https://doi.org/10.1002/adma.202400301.
36. Slonczewski, J.C. (1996). Current-driven excitation of magnetic multilayers. J. Magn. Magn Mater. *159*, L1–L7. https://doi.org/10.1016/0304-8853(96)00062-5.
37. Berger, L. (1996). Emission of spin waves by a magnetic multilayer traversed by a current. Phys. Rev. B *54*, 9353–9358. https://doi.org/10.1103/PhysRevB.54.9353.
38. Boulle, O., Cros, V., Groller, J., Pereira, L.G., Deranlot, C., Petroff, F., Faini, G., Barnaś, J., and Fert, A. (2007). Shaped angular dependence of the spin-transfer torque and microwave generation without magnetic field. Nat. Phys. *3*, 492. https://doi.org/10.1038/nphys618.
39. Kubota, H., Fukushima, A., Yakushiji, K., Nagahama, T., Yuasa, S., Ando, K., Maehara, H., Nagamine, Y., Tsunekawa, K., Djayaprawira, D.D., et al. (2008). Quantitative measurement of voltage dependence of spin-transfer torque in MgO-based magnetic tunnel junctions. Nat. Phys. *4*, 37–41. https://doi.org/10.1038/nphys784.
40. Deac, A.M., Fukushima, A., Kubota, H., Maehara, H., Suzuki, Y., Yuasa, S., Nagamine, Y., Tsunekawa, K., Djayaprawira, D.D., and Watanabe, N. (2008). Bias-driven high-power microwave emission from MgO-based tunnel magnetoresistance devices. Nat. Phys. *4*, 803–809. https://doi.org/10.1038/nphys1036.
41. Dieny, B., Prejbeanu, I.L., Garello, K., Gambardella, P., Freitas, P., Lehndorff, R., Raberg, W., Ebels, U., Demokritov, S.O., Akerman, J., et al. (2020). Opportunities and challenges for spintronics in the microelectronics industry. Nat. Electron. *3*, 446–459. https://doi.org/10.1038/s41928-020-0461-5.
42. Hirohata, A. (2022). MRAM makes its mark. Nat. Electron. *5*, 832–833. https://doi.org/10.1038/s41928-022-00893-w.
43. Sun, J.Z. (2000). Spin-current interaction with a monodomain magnetic body: A model study. Phys. Rev. B *62*, 570–578. https://doi.org/10.1103/PhysRevB.62.570.
44. Pribiag, V.S., Krivorotov, I.N., Fuchs, G.D., Braganca, P.M., Ozatay, O., Sankey, J.C., Ralph, D.C., and Buhrman, R.A. (2007). Magnetic vortex oscillator driven by d.c. spin-polarized current. Nat. Phys. *3*, 498–503. https://doi.org/10.1038/nphys619.
45. Yamada, K., Kasai, S., Nakatani, Y., Kobayashi, K., Kohno, H., Thiaville, A., and Ono, T. (2007). Electrical switching of the vortex core in a magnetic disk. Nat. Mater. *6*, 269. https://doi.org/10.1038/nmat1867.
46. Zhu, J.-G.,, Zhu, X., and Tang, Y. (2008). Microwave assisted magnetic recording. IEEE Trans. Magn. *44*, 125–131. https://doi.org/10.1109/TMAG.2007.911031.
47. Seki, T., Utsumiya, K., Nozaki, Y., Imamura, H., and Takanashi, K. (2013). Spin wave-assisted reduction in switching field of highly coercive iron-platinum magnets. Nat. Commun. *4*, 1726. https://doi.org/10.1038/ncomms2737.
48. Nguyen, T.V.A., Naganuma, H., Honjo, H., Ikeda, S., and Endoh, T. (2024). Ultrafast spin–orbit torque-induced magnetization switching in a 75°-canted magnetic tunnel junction. AIP Adv. *14*, 025018. https://doi.org/10.1063/9.0000789.
49. Lee, K.-S., Lee, S.-W., Min, B.-C., and Lee, K.-J. (2013). Threshold current for switching of a perpendicular magnetic layer induced by spin Hall effect. Appl. Phys. Lett. *102*, 112410. https://doi.org/10.1063/1.4798288.

50. Miron, I.M., Garello, K., Gaudin, G., Zermatten, P.-J., Costache, M.V., Auffret, S., Bandiera, S., Rodmacq, B., Schuhl, A., and Gambardella, P. (2011). Perpendicular switching of a single ferromagnetic layer induced by in-plane current injection. Nature *476*, 189–193. https://doi.org/10.1038/nature10309.

51. Garello, K., Yasin, F., Couet, S., Souriau, L., Swerts, J., Rao, S., Van Beek, S., Kim, W., Liu, E., Kundu, S., et al. (2018). SOT-MRAM 300MM Integration for Low Power and Ultrafast Embedded Memories. IEEE Symp. VLSI Circuits *81*, 81–82. https://doi.org/10.1109/VLSIC.2018.8502269.

52. Liu, L., Pai, C.-F., Ralph, D.C., and Buhrman, R.A. (2012). Magnetic oscillations driven by the spin Hall effect in 3-terminal magnetic tunnel junction devices. Phys. Rev. Lett. *109*, 186602. https://doi.org/10.1103/PhysRevLett.109.186602.

53. Dzyaloshinskii, I. (1958). A thermodynamic theory of "weak" ferromagnetism of antiferromagnetics. J. Phys. Chem. Solid. *4*, 241. https://doi.org/10.1016/0022-3697(58)90076-3.

54. Moriya, T. (1960). Anisotropic superexchange interaction and weak ferromagnetism. Phys. Rev. *120*, 91–98. https://doi.org/10.1103/PhysRev.120.91.

55. Camley, R.E., and Livesey, K.L. (2023). Consequences of the Dzyaloshinskii-Moriya interaction. Surf. Sci. Rep. *78*, 100605. https://doi.org/10.1016/j.surfrep.2023.100605.

56. Skyrme, T.H.R. (1958). A non-linear theory of strong interactions. Proc. Royal Soc. London A: Math. Phys. Eng. Sci. *247*, 260. https://doi.org/10.1098/rspa.1958.0183.

57. Skyrme, T.H.R. (1959). A unified model of K- and π-mesons236. Proc. R. Soc. Lond. A *252*, 252. https://doi.org/10.1098/rspa.1959.0149.

58. Skyrme, T.H.R. (1961). A non-linear field theory. Proc. R. Soc. Lond. A *260*, 127–138. https://doi.org/10.1098/rspa.1961.0018.

59. Skyrme, T.H.R. (1961). Particle states of a quantized meson field. Proc. R. Soc. Lond. A *262*, 237–245. https://doi.org/10.1098/rspa.1961.0115.

60. Mühlbauer, S., Binz, B., Jonietz, F., Pfleiderer, C., Rosch, A., Neubauer, A., Georgii, R., and Böni, P. (2009). Skyrmion lattice in a chiral magnet. Science *323*, 915–919. https://doi.org/10.1126/science.1166767.

61. Chumak, A.V., Vasyuchka, V.I., Serga, A.A., and Hillebrands, B. (2015). Magnon spintronics. Nat. Phys. *11*, 453–461. https://doi.org/10.1038/nphys3347.

62. Nakatani, Y., Yamada, K., and Hirohata, A. (2019). Switching of Skyrmion chirality by local heating. Sci. Rep. *9*, 13475. https://doi.org/10.1038/s41598-019-49875-7.

63. Pham, V.T., Sisodia, N., Di Manici, I., Urrestarazu-Larrañaga, J., Bairagi, K., Pelloux-Prayer, J., Guedas, R., Buda-Prejbeanu, L.D., Auffret, S., Locatelli, A., et al. (2024). Fast current-induced skyrmion motion in synthetic antiferromagnets. Science *384*, 307–312. https://doi.org/10.1126/science.add5751.

64. Tainosho, T., Inoue, J.i., Sharmin, S., Takeguchi, M., Kita, E., and Yanagihara, H. (2019). Large negative uniaxial magnetic anisotropy in highly distorted Co-ferrite thin films. Appl. Phys. Lett. *114*, 092408. https://doi.org/10.1063/1.5064845.

65. Vlaminck, V., and Bailleul, M. (2008). Current-induced spin-wave Doppler shift. Science *322*, 410–413. https://doi.org/10.1126/science.1162843.

66. Uchida, K., Takahashi, S., Harii, K., Ieda, J., Koshibae, W., Ando, K., Maekawa, S., and Saitoh, E. (2008). Observation of the spin Seebeck effect. Nature *455*, 778–781. https://doi.org/10.1038/nature07321.

67. Xiao, J., Bauer, G.E.W., Uchida, K.-c., Saitoh, E., and Maekawa, S. (2010). Theory of magnon-driven spin Seebeck effect. Phys. Rev. B *81*, 214418. https://doi.org/10.1103/PhysRevB.81.214418.

68. Adachi, H., Ohe, J.-i., Takahashi, S., and Maekawa, S. (2011). Linear-response theory of spin Seebeck effect in ferromagnetic insulators. Phys. Rev. B *83*, 094410. https://doi.org/10.1103/PhysRevB.83.094410.

69. Bauer, G.E.W., Saitoh, E., and Van Wees, B.J. (2012). Spin caloritronics. Nat. Mater. *11*, 391–399. https://doi.org/10.1038/nmat3301.

70. Uchida, K., Xiao, J., Adachi, H., Ohe, J., Takahashi, S., Ieda, J., Ota, T., Kajiwara, Y., Umezawa, H., Kawai, H., et al. (2010). Spin Seebeck insulator. Nat. Mater. *9*, 894–897. https://doi.org/10.1038/nmat2856.

71. Uchida, K., Adachi, H., An, T., Ota, T., Toda, M., Hillebrands, B., Maekawa, S., and Saitoh, E. (2011). Long-range spin Seebeck effect and acoustic spin pumping. Nat. Mater. *10*, 737–741. https://doi.org/10.1038/nmat3099.

72. Jaworski, C.M., Yang, J., Mack, S., Awschalom, D.D., Heremans, J.P., and Myers, R.C. (2010). Observation of the spin-Seebeck effect in a ferromagnetic semiconductor. Nat. Mater. *9*, 898–903. https://doi.org/10.1038/nmat2860.

73. For a detailed review of recent advances in this area, see, for example Kikkawa, T., and Saitoh, E. (2023). Spin Seebeck effect: Sensitive probe for elementary excitation, spin correlation, transport, magnetic order, and domains in solids. Annu. Rev. Condens. Matter Phys. *14*, 129–151. https://doi.org/10.1146/annurev-conmatphys-040721-014957.

74. Flipse, J., Dejene, F.K., Wagenaar, D., Bauer, G.E.W., Ben Youssef, J., and van Wees, B.J. (2014). Observation of the spin Peltier effect for magnetic insulators. Phys. Rev. Lett. *113*, 027601. https://doi.org/10.1103/PhysRevLett.113.027601.

75. Basso, V., Ferraro, E., Magni, A., Sola, A., Kuepferling, M., and Pasquale, M. (2016). Nonequilibrium thermodynamics of the spin Seebeck and spin Peltier effects. Phys. Rev. B *93*, 184421. https://doi.org/10.1103/PhysRevB.93.184421.

76. Daimon, S., Iguchi, R., Hioki, T., Saitoh, E., and Uchida, K.-i. (2016). Thermal imaging of spin Peltier effect. Nat. Commun. *7*, 13754. https://doi.org/10.1038/ncomms13754.

77. Ohnuma, Y., Matsuo, M., and Maekawa, S. (2017). Theory of the spin Peltier effect. Phys. Rev. B *96*, 134412. https://doi.org/10.1103/PhysRevB.96.134412.

78. Qiu, Z., Li, J., Hou, D., Arenholz, E., N'Diaye, A.T., Tan, A., Uchida, K.-i., Sato, K., Okamoto, S., Tserkovnyak, Y., et al. (2016). Spin-current probe for phase transition in an insulator. Nat. Commun. *7*, 12670. https://doi.org/10.1038/ncomms12670.

79. Kikkawa, T., Shen, K., Flebus, B., Duine, R.A., Uchida, K.I., Qiu, Z., Bauer, G.E.W., and Saitoh, E. (2016). Magnon polarons in the spin Seebeck effect. Phys. Rev. Lett. *117*, 207203. https://doi.org/10.1103/PhysRevLett.117.207203.

80. Maehrlein, S.F., Radu, I., Maldonado, P., Paarmann, A., Gensch, M., Kalashnikova, A.M., Pisarev, R.V., Wolf, M., Oppeneer, P.M., Barker, J., and Kampfrath, T. (2018). Dissecting spin-phonon equilibration in ferrimagnetic insulators by ultrafast lattice excitation. Sci. Adv. *4*, aar5164. https://doi.org/10.1126/sciadv.aar5164.

81. Yamazaki, T., Iguchi, T., Ohkubo, T., Nagano, H., and Uchida, K. (2020). Transient response of the spin Peltier effect revealed by lock-in thermoreflectance measurements. Phys. Rev. B *101*, 020415. https://doi.org/10.1103/PhysRevB.101.020415.

82. Uchida, K., Adachi, H., Kikuchi, D., Ito, S., Qiu, Z., Maekawa, S., and Saitoh, E. (2015). Generation of spin currents by surface plasmon resonance. Nat. Commun. *6*, 5910. https://doi.org/10.1038/ncomms6910.

83. Ishii, S., Uchida, K.-i., Dao, T.D., Wada, Y., Saitoh, E., and Nagao, T. (2017). Wavelength-selective spin-current generator using infrared plasmonic metamaterials. APL Photonics *2*, 106103. https://doi.org/10.1063/1.4991438.

84. Shilina, P.V., Ignatyeva, D.O., Kapralov, P.O., Sekatskii, S.K., Nur-E-Alam, M., Vasiliev, M., Alameh, K., Achanta, V.G., Song, Y., Hamidi, S. M., et al. (2021). Nanophotonic structures with optical surface modes for tunable spin current generation. Nanoscale *13*, 5791–5799. https://doi.org/10.1039/D0NR08692D.

85. Fan, Y., Cao, G., Jiang, S., Åkerman, J., and Åkerman, J. (2025). Spatiotemporal observation of surface plasmon polariton mediated ultrafast demagnetization. Nat. Commun. *16*, 873. https://doi.org/10.1038/s41467-025-56158-5.

86. Kuznetsov, N., Qin, H., Flajšman, L., and van Dijken, S. (2025). Optical control of spin waves in hybrid magnonic-plasmonic structures. Sci. Adv. *11*, eads2420. https://doi.org/10.1126/sciadv.ads2420.
87. Al Saidi, W., Sbiaa, R., Dusch, Y., and Tiercelin, N. (2024). Plasmon-driven creation of magnetic topological structures. Appl. Phys. Lett. *124*, 242402. https://doi.org/10.1063/5.0208694.
88. Maier, S.A. (2007). Plasmonics: Fundamentals and Applications (Berlin: Springer Science & Business Media). https://doi.org/10.1007/0-387-37825-1.
89. Sambles, J.R., Bradbery, G.W., and Yang, F. (1991). Optical excitation of surface plasmons: An introduction. Contemp. Phys. *32*, 173–183. https://doi.org/10.1080/00107519108211048.
90. Kim, K.-Y., Lee, I.-M., Kim, J., Jung, J., and Lee, B. (2012). Time reversal and the spin angular momentum of transverse-electric and transverse-magnetic surface modes. Phys. Rev. *86*, 063805. https://doi.org/10.1103/PhysRevA.86.063805.
91. Bliokh, K.Y., and Nori, F. (2012). Transverse spin of a surface polariton. Phys. Rev. *85*, 061801. https://doi.org/10.1103/PhysRevA.85.061801.
92. Canaguier-Durand, A., and Genet, C. (2014). Transverse spinning of a sphere in a plasmonic field. Phys. Rev. *89*, 033841. https://doi.org/10.1103/PhysRevA.89.033841.
93. Bliokh, K.Y., Bekshaev, A.Y., and Nori, F. (2017). Optical momentum and angular momentum in complex media: from the Abraham–Minkowski debate to unusual properties of surface plasmon-polaritons. New J. Phys. *19*, 123014. https://doi.org/10.1088/1367-2630/aa8913.
94. Hertel, R. (2006). Theory of the inverse Faraday effect in metals. J. Magn. Magn Mater. *303*, L1–L4. https://doi.org/10.1016/j.jmmm.2005.10.225.
95. Zhang, H.-L., Wang, Y.-Z., and Chen, X.-J. (2009). A simple explanation for the inverse Faraday effect in metals. J. Magn. Magn Mater. *321*, L73–L74. https://doi.org/10.1016/j.jmmm.2009.08.023.
96. Oue, D., and Matsuo, M. (2020). Effects of surface plasmons on spin currents in a thin film system. New J. Phys. *22*, 033040. https://doi.org/10.1088/1367-2630/ab764c.
97. Oue, D., and Matsuo, M. (2020). Electron spin transport driven by surface plasmon polaritons. Phys. Rev. B *101*, 161404(R). https://doi.org/10.1103/PhysRevB.101.161404.
98. Oue, D., and Matsuo, M. (2020). Optically induced electron spin currents in the Kretschmann configuration. Phys. Rev. B *102*, 125431. https://doi.org/10.1103/PhysRevB.102.125431.
99. Bekshaev, A.Y. (2022). Spin-accumulation and spin-transport effects induced by surface plasmon-polariton waves. J. Opt. Soc. Am. B *39*, 3187. https://doi.org/10.1364/JOSAB.475331.
100. Ukhtary, M.S., Tian, Y., and Saito, R. (2021). Spin current generation by edge plasmons in graphene ribbons. Phys. Rev. B *103*, 245428. https://doi.org/10.1103/PhysRevB.103.245428.
101. Tian, Y., Ukhtary, M.S., and Saito, R. (2022). Switching performance of optically generated spin current at the graphene edge. Phys. Rev. B *106*, 045420. https://doi.org/10.1103/PhysRevB.106.045420.
102. Zhang, L., Zeng, X., Zhang, D., Wen, T., Zhong, Z., Zhang, H., and Jin, L., (2024). Surface plasmon resonance enhanced terahertz spin current emission in Au nanoparticles/ferromagnet thin film heterostructure. Appl. Phys. Lett. *125*, 152401. https://doi.org/10.1063/5.0231140.
103. Uchida, K.i., An, T., Kajiwara, Y., Toda, M., and Saitoh, E. (2011). Surface-acoustic-wave-driven spin pumping in $Y_3Fe_5O_{12}$/Pt hybrid structure. Appl. Phys. Lett. *99*, 212501. https://doi.org/10.1063/1.3662032.
104. Uchida, K., Adachi, H., An, T., Nakayama, H., Toda, M., Hillebrands, B., Maekawa, S., and Saitoh, E. (2012). Acoustic spin pumping: Direct generation of spin currents from sound waves in Pt/$Y_3Fe_5O_{12}$ hybrid structures. J. Appl. Phys. *111*, 053903. https://doi.org/10.1063/1.3688332.
105. Weiler, M., Dreher, L., Heeg, C., Huebl, H., Gross, R., Brandt, M.S., and Goennenwein, S.T.B. (2011). Elastically driven ferromagnetic resonance in Nickel thin films. Phys. Rev. Lett. *106*, 117601. https://doi.org/10.1103/PhysRevLett.106.117601.
106. Dreher, L., Weiler, M., Pernpeintner, M., Huebl, H., Gross, R., Brandt, M. S., and Goennenwein, S.T.B. (2012). Surface acoustic wave driven ferromagnetic resonance in nickel thin films: Theory and experiment. Phys. Rev. B *86*, 134415. https://doi.org/10.1103/PhysRevB.86.134415.
107. Weiler, M., Huebl, H., Goerg, F.S., Czeschka, F.D., Gross, R., and Goennenwein, S.T.B. (2012). Spin pumping with coherent elastic waves. Phys. Rev. Lett. *108*, 176601. https://doi.org/10.1103/PhysRevLett.108.176601.
108. Xu, M., Yamamoto, K., Puebla, J., Baumgaertl, K., Rana, B., Miura, K., Takahashi, H., Grundler, D., Maekawa, S., and Otani, Y. (2020). Nonreciprocal surface acoustic wave propagation via magneto-rotation coupling. Sci. Adv. *6*, eabb1724. https://doi.org/10.1126/sciadv.abb1724.
109. Barnett, S.J. (1915). Magnetization by rotation. Phys. Rev. *6*, 239–270. https://doi.org/10.1103/PhysRev.6.239.
110. Einstein, A., and de Haas, W.J. (1915). Experimental proof of the existence of Ampère's molecular currents. Roy. Netherlands Acad. Arts Sci. (KNAW) Proc. *18*, 696.
111. Barnett, S.J. (1935). Gyromagnetic and electron-inertia effects. Rev. Mod. Phys. *7*, 129–166. https://doi.org/10.1103/RevModPhys.7.129.
112. Scott, G.G. (1962). Review of gyromagnetic ratio experiments. Rev. Mod. Phys. *34*, 102–109. https://doi.org/10.1103/RevModPhys.34.102.
113. Topper, D.R. (2007). Quirky Sides of Scientists: True Tales of Ingenuity and Error from Physics and Astronomy (New York, USA: Springer). https://doi.org/10.1007/978-0-387-71019-8.
114. Hehl, F.W., and Ni, W.-T. (1990). Inertial effects of a Dirac particle. Phys. Rev. D *42*, 2045–2048. https://doi.org/10.1103/PhysRevD.42.2045.
115. Matsuo, M., Ieda, J., Saitoh, E., and Maekawa, S. (2011). Effects of mechanical rotation on spin currents. Phys. Rev. Lett. *106*, 076601. https://doi.org/10.1103/PhysRevLett.106.076601.
116. Matsuo, M., Ieda, J., Harii, K., Saitoh, E., and Maekawa, S. (2013). Mechanical generation of spin current by spin-rotation coupling. Phys. Rev. B *87*, 180402(R). https://doi.org/10.1103/PhysRevB.87.180402.
117. Wallis, T.M., Moreland, J., and Kabos, P. (2006). Einstein-de Haas effect in a NiFe film deposited on a microcantilever. Appl. Phys. Lett. *89*, 122502. https://doi.org/10.1063/1.2355445.
118. Zolfagharkhani, G., Gaidarzhy, A., Degiovanni, P., Kettemann, S., Fulde, P., and Mohanty, P. (2008). Nanomechanical detection of itinerant electron spin flip. Nat. Nanotechnol. *3*, 720–723. https://doi.org/10.1038/nnano.2008.311.
119. Dornes, C., Acremann, Y., Savoini, M., Kubli, M., Neugebauer, M.J., Abreu, E., Huber, L., Lantz, G., Vaz, C.A.F., Lemke, H., et al. (2019). The ultrafast Einstein–de Haas effect. Nature *565*, 209–212. https://doi.org/10.1038/s41586-018-0822-7.
120. Mori, K., Dunsmore, M.G., Losby, J.E., Jenson, D.M., Belov, M., and Freeman, M.R. (2020). Einstein-de Haas effect at radio frequencies in and near magnetic equilibrium. Phys. Rev. B *102*, 054415. https://doi.org/10.1103/PhysRevB.102.054415.
121. Ono, M., Chudo, H., Harii, K., Okayasu, S., Matsuo, M., Ieda, J., Takahashi, R., Maekawa, S., and Saitoh, E. (2015). Barnett effect in paramagnetic states. Phys. Rev. B *92*, 174424. https://doi.org/10.1103/PhysRevB.92.174424.
122. Ogata, Y., Chudo, H., Ono, M., Harii, K., Matsuo, M., Maekawa, S., and Saitoh, E. (2017). Gyroscopic g factor of rare earth metals. Appl. Phys. Lett. *110*, 072409. https://doi.org/10.1063/1.4976998.
123. Imai, M., Ogata, Y., Chudo, H., Ono, M., Harii, K., Matsuo, M., Ohnuma, Y., Maekawa, S., and Saitoh, E. (2018). Observation of gyromagnetic reversal. Appl. Phys. Lett. *113*, 052402. https://doi.org/10.1063/1.5041464.
124. Imai, M., Chudo, H., Ono, M., Harii, K., Matsuo, M., Ohnuma, Y., Maekawa, S., and Saitoh, E. (2019). Angular momentum compensation manipulation to room temperature of the ferrimagnet $Ho_{3-x}Dy_xFe_5O_{12}$ detected by the Barnett effect. Appl. Phys. Lett. *114*, 162402. https://doi.org/10.1063/1.5095166.

125. Takahashi, R., Matsuo, M., Ono, M., Harii, K., Chudo, H., Okayasu, S., Ieda, J., Takahashi, S., Maekawa, S., and Saitoh, E. (2016). Spin hydrodynamic generation. Nat. Phys. *12*, 52–56. https://doi.org/10.1038/nphys3526.

126. Takahashi, R., Chudo, H., Matsuo, M., Harii, K., Ohnuma, Y., Maekawa, S., and Saitoh, E. (2020). Giant spin hydrodynamic generation in laminar flow. Nat. Commun. *11*, 3009. https://doi.org/10.1038/s41467-020-16753-0.

127. Sung, Y., Lue, N., Hamza, B., Martel, J., Irimia, D., Dasari, R.R., Choi, W., Yaqoob, Z., and So, P. (2014). Three-dimensional holographic refractive-index measurement of continuously flowing cells in a microfluidic channel. Phys. Rev. Appl. *1*, 014002. https://doi.org/10.1103/PhysRevApplied.1.014002.

128. Tabaei Kazerooni, H., Zinchenko, G., Schumacher, J., and Cierpka, C. (2021). Electrical voltage by electron spin-vorticity coupling in laminar ducts. Phys. Rev. Fluids *6*, 043703. https://doi.org/10.1103/PhysRevFluids.6.043703.

129. Kobayashi, D., Yoshikawa, T., Matsuo, M., Iguchi, R., Maekawa, S., Saitoh, E., and Nozaki, Y. (2017). Spin current generation using a surface acoustic wave generated via spin-rotation coupling. Phys. Rev. Lett. *119*, 077202. https://doi.org/10.1103/PhysRevLett.119.077202.

130. Kurimune, Y., Matsuo, M., Maekawa, S., and Nozaki, Y. (2020). Highly nonlinear frequency-dependent spin-wave resonance excited via spin-vorticity coupling. Phys. Rev. B *102*, 174413. https://doi.org/10.1103/PhysRevB.102.174413.

131. Tateno, S., Okano, G., Matsuo, M., and Nozaki, Y. (2020). Electrical evaluation of the alternating spin current generated via spin-vorticity coupling. Phys. Rev. B *102*, 104406. https://doi.org/10.1103/PhysRevB.102.104406.

132. Kurimune, Y., Matsuo, M., and Nozaki, Y. (2020). Observation of gyromagnetic spin wave resonance in NiFe films. Phys. Rev. Lett. *124*, 217205. https://doi.org/10.1103/PhysRevLett.124.217205.

133. Tateno, S., Kurimune, Y., Matsuo, M., Yamanoi, K., and Nozaki, Y. (2021). Einstein–de Haas phase shifts in surface acoustic waves. Phys. Rev. B *104*, L020404. https://doi.org/10.1103/PhysRevB.104.L020404.

134. Hirohata, A., Baba, Y., Murphy, B.A., Ng, B., Yao, Y., Nagao, K., and Kim, J.-y. (2018). Magneto-optical detection of spin accumulation under the influence of mechanical rotation. Sci. Rep. *8*, 1974. https://doi.org/10.1038/s41598-018-20269-5.

135. Harii, K., Seo, Y.-J., Tsutsumi, Y., Chudo, H., Oyanagi, K., Matsuo, M., Shiomi, Y., Ono, T., Maekawa, S., and Saitoh, E. (2019). Spin Seebeck mechanical force. Nat. Commun. *10*, 2616. https://doi.org/10.1038/s41467-019-10625-y.

136. Wood, A.A., Lilette, E., Fein, Y.Y., Tomek, N., McGuinness, L.P., Hollenberg, L.C.L., Scholten, R.E., and Martin, A.M. (2018). Quantum measurement of a rapidly rotating spin qubit in diamond. Sci. Adv. *4*, eaar7691. https://doi.org/10.1126/sciadv.aar7691.

137. Chudo, H., Ono, M., Harii, K., Matsuo, M., Ieda, J., Haruki, R., Okayasu, S., Maekawa, S., Yasuoka, H., and Saitoh, E. (2014). Observation of Barnett fields in solids by nuclear magnetic resonance. APEX *7*, 063004. https://doi.org/10.7567/APEX.7.063004.

138. Chudo, H., Harii, K., Matsuo, M., Ieda, J., Ono, M., Maekawa, S., and Saitoh, E. (2015). Rotational Doppler effect and Barnett field in spinning NMR. J. Phys. Soc. Jpn. *84*, 043601. https://doi.org/10.7566/JPSJ.84.043601.

139. Harii, K., Chudo, H., Ono, M., Matsuo, M., Ieda, J., Okayasu, S., Maekawa, S., and Saitoh, E. (2015). Line splitting by mechanical rotation in nuclear magnetic resonance. Jpn. J. Appl. Phys. *54*, 050302. https://doi.org/10.7567/JJAP.54.050302.

140. Chudo, H., Matsuo, M., Maekawa, S., and Saitoh, E. (2021). Barnett field, rotational Doppler effect, and Berry phase studied by nuclear quadrupole resonance with rotation. Phys. Rev. B *103*, 174308. https://doi.org/10.1103/PhysRevB.103.174308.

141. Wood, A. ., Lilette, E., Fein, Y.Y., Perunicic, V.S., Hollenberg, L. . ., Scholten, R.E., and Martin, A.M. (2017). Magnetic pseudo-fields in a rotating electron–nuclear spin system. Nat. Phys. *13*, 1070–1073. https://doi.org/10.1038/nphys4221.

142. Adamczyk, L., Adkins, J., Agakishiev, G., Aggarwal, M., Ahammed, Z., Ajitanand, N., Alekseev, I., Anderson, D., Aoyama, R., Aparin, A., et al. (2017). Global Λ hyperon polarization in nuclear collisions. Nature *548*, 62. https://doi.org/10.1038/nature23004.

143. Adam, J., Adamczyk, L., Adams, J.R., Adkins, J.K., Agakishiev, G., Aggarwal, M.M., Ahammed, Z., Ajitanand, N.N., Alekseev, I., Anderson, D. M., et al. (2018). The STAR Collaboration) (2018). Global polarization of hyperons in Au + Au collisions at GeV. Phys. Rev. C *98*, 014910. https://doi.org/10.1103/PhysRevC.98.014910.

144. Adam, J., Adamczyk, L., Adams, J.R., Adkins, J.K., Agakishiev, G., Aggarwal, M.M., Ahammed, Z., Alekseev, I., Anderson, D.M., Aoyama, R., et al. (2019). Polarization of Λ ($\bar{\Lambda}$) hyperons along the beam direction in Au+Au collisions at $\sqrt{S_{NN}}$=200 GeV. Phys. Rev. Lett. *123*, 132301.

145. Acharya, S., Adamová, D., Adler, A., Adolfsson, J., Aggarwal, M.M., Aglieri Rinella, G., Agnello, M., Agrawal, N., Ahammed, Z., Ahmad, S., et al. (2020). Evidence of spin-orbital angular momentum interactions in relativistic heavy-ion collisions. Phys. Rev. Lett. *125*, 012301. https://doi.org/10.1103/PhysRevLett.125.012301.

146. Adam, J., Adamczyk, L., Adams, J.R., Adkins, J.K., Agakishiev, G., Aggarwal, M.M., Ahammed, Z., Alekseev, I., Anderson, D.M., Aparin, A., et al. (2021). The STAR Collaboration) (2021). Global polarization of Ξ and Ω hyperons in Au+Au collisions at $\sqrt{S_{NN}}$=200 GeV. Phys. Rev. Lett. *126*, 162301. https://doi.org/10.1103/PhysRevLett.126.162301.

147. Tokoro, M., and Takahashi, R. (2022). Spin hydrodynamic generation in low-melting-point pure metal. Phys. Rev. Appl. *17*, L061003. https://doi.org/10.1103/PhysRevApplied.17.L061003.